Supplementary Information

Quantum annealing of a well-defined frustrated magnet

Yuqian Zhao, Zhaohua Ma, Zhangzhen He, Haijun Liao, Junfeng Wang, and Yuesheng Li

Supplementary Note 1. Principal axes of the effective Ising spin system of α-CoV_2O_6

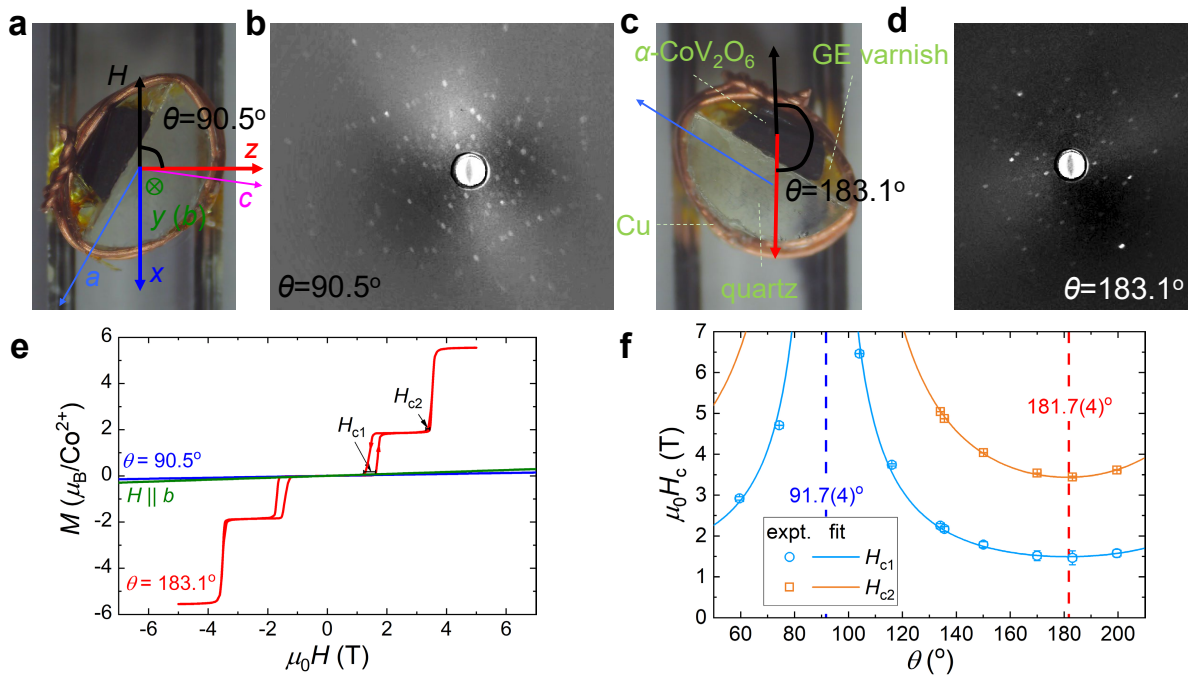

Supplementary Fig. 1 | Magnetization measured on the single crystal of α-CoV_2O_6. a, **c**, Images of the crystal at rotation angles, θ = 90.5° and 183.1°, respectively. **b**, **d**, The rotation angles were determined by Laue x-ray diffraction measurements and further confirmed with microscopic images (e.g., **a**, **c**), with a maximum error of $\sim \pm 1°$. **e**, Magnetization measured at θ = 90.5° and 183.1° and at 5 K. The critical fields (H_{c1} and H_{c2}) are indicated, and the magnetization measured along the b axis is displayed for comparison. **f**, Rotation-angle dependence of H_{c1} and H_{c2} measured at 5 K. The solid lines represent the combined fit to the experimental data using Supplementary Eq. (1), and the dashed blue and red lines show the positions of the other two principal axes as determined by the fit, with $H_{c1} = \infty$ ($H_{c2} = \infty$) and $H_{c1} = H_{c1}^{z}$ ($H_{c2} = H_{c2}^{z}$), respectively. Error bars, 1σ s.e.

High-quality single crystals of α-CoV_2O_6 (space group: $C121$) were grown using the flux method [1–3]. The nonmagnetic reference compound α-ZnV_2O_6 used to measure the lattice specific heat was synthesized through a traditional solid-phase method using stoichiometric mixtures of $ZnC_2O_4{\cdot}2H_2O$ and V_2O_5 in air up to 630 °C for 60 hours, with intermediate grinding. The phase purity of the sample was verified by

x-ray diffraction. Due to the strong (Ising) anisotropy of the magnetism of the α-CoV_2O_6 spin system [4, 5], the single crystals were cut to the appropriate size in our measurements to maintain a high signal-to-noise ratio while avoiding excessive stress. For all magnetization measurements in a magnetic properties measurement system (MPMS) up to 7 T, we selected a single crystal weighing 10.52 mg with a natural surface corresponding to the ab plane (0 0 1), as confirmed by Laue x-ray diffraction. The crystal was affixed to a quartz sample holder with GE varnish and cooper wire (Cu $\geq$ 99.999%), as depicted in Supplementary Fig. 1a,c. We verified the orientation and position of the crystal following each MPMS measurement, and no movement relative to the sample holder was detected. In α-CoV_2O_6, the two-fold rotation axis is oriented along the b direction, indicating that b must be one of the three principal axes (i.e., the y axis), while the other two principal axes are orthogonal to the b axis. Supplementary Fig. 1e displays the magnetization measured along the b axis, which exhibits a linear field dependence at least up to 7 T, consistent with the findings reported in previous references [1, 3]. This observation confirms the designation of b as one of the principal axes.

Lenertz et al. reported that at low temperatures the magnetic moments (i.e., Ising spins) of Co^{2+} in α-CoV_2O_6 are aligned along the CoO_6 octahedra axis (z, which is perpendicular to b), as determined by neutron diffraction measurements performed under various applied magnetic fields [4]. To confirm this, we performed magnetization measurements perpendicular to the b axis by rotating the crystal through an angle θ, as illustrated in Supplementary Fig. 1. Here, θ is the angle between the z axis (i.e., the Ising axis) and the direction of the applied magnetic field (H). At 5 K, we observed two critical fields, H_{c1} and H_{c2}, consistent with previous reports in Ref. [1]. These critical fields are associated with the successive transitions among the three phases characterized by M^z = 0 (interchain antiferromagnetic), g^z/6 (1/3-plateau), and g^z/2 (fully polarized), respectively [4, 5]. The dependence of these critical fields on θ was calculated for the crystal of α-CoV_2O_6, as

$$H_{c1} = \frac{H_{c1}^z}{|\cos(\theta - \theta_0)|}, \;\; H_{c2} = \frac{H_{c2}^z}{|\cos(\theta - \theta_0)|}, \tag{1}$$

where $\mu_0 H_{c1}^z \sim 1.49$ T and $\mu_0 H_{c2}^z \sim 3.44$ T are the minimum values of $\mu_0 H_{c1}$ and $\mu_0 H_{c2}$, respectively, and θ_0 represents the offset of θ. Our combined fit to the experimental data yielded a small offset angle of $\theta_0 = 1.7 \pm 0.4^\circ$ (see Supplementary Fig. 1f), consistent with the previous neutron diffraction work [4].

For the effective Ising spin system of α-CoV_2O_6, we define a rectangular coordinate system with the principal axes, x, y, and z, as shown in Supplementary Fig. 1a and Supplementary Fig. 4a.

Supplementary Note 2. Crystal-field Hamiltonian with spin-orbit coupling in α-CoV_2O_6

We investigate the single-ion interactions in α-CoV_2O_6 to understand the relationship between the applied transverse magnetic field $\mu_0 H^{\perp}$ (in T) and the resulted transverse field Γ (in K). The crystalline electric field (CEF) of Co^{2+} is primarily determined by the local CoO_6 environment [6]. The CoO_6 octahedra possess approximate C_{2v} point-group symmetry (see Supplementary Fig. 4a). The crystal structure of α-CoV_2O_6 is two-fold rotation symmetrical about the y axis, and the dihedral angle of O1–Co-Co–O2 (with Co-Co along the y axis) is 90.04° close to a right angle [1], resulting in good mirror symmetries on both xy and yz planes for the CoO_6 octahedra. Therefore, we start with the single-ion Hamiltonian that is invariant under the C_{2v} point-group symmetry [7],

$$\mathcal{H}_{\rm SI} = B_2^0 O_2^0 + B_2^2 O_2^2 + B_4^0 O_4^0 + B_4^2 O_4^2 + B_4^4 O_4^4 + B_6^0 O_6^0 + B_6^2 O_6^2 + + B_6^4 O_6^4 + B_6^6 O_6^6 + \lambda \mathbf{s}\cdot\mathbf{L} - \mu_0\mu_B \mathbf{H}\cdot(2\mathbf{s}+\mathbf{L}), \quad (2)$$

where B_n^m (m, n are integers and $m \leq n$) are CEF parameters, O_n^m are the Stevens operators, and λ = -22.32 meV the spin-orbit ($\mathbf{s}$-$\mathbf{L}$) coupling [8, 9]. For Co^{2+}, s = 3/2 and L = 3 give rise to a $(2s+1)(2L+1)$ = 28 dimensional Hilbert space of $\mathcal{H}_{\rm SI}$. By diagonalizing $\mathcal{H}_{\rm SI}$, we obtain the eigenvalues and eigenvectors, E_j and $|E_j\rangle$ (j = 1, ..., 28), respectively. The single-ion dc magnetic susceptibility is calculated by,

$$\chi_{\rm SI}^{\alpha} = \frac{N_{\rm A}\mu_{\rm B}\sum_{j=1}^{28}\exp(-\frac{E_j}{k_{\rm B}T})\langle E_j|2s^{\alpha}+L^{\alpha}|E_j\rangle}{H^{\alpha}\sum_{j=1}^{28}\exp(-\frac{E_j}{k_{\rm B}T})}, \quad (3)$$

where α = x', y', z' in the CEF coordinate system with x' = x, y' = z, z' = $-y$ (see Supplementary Fig. 4a for the definition of the xyz coordinate system). It is noteworthy that the small transverse susceptibilities (measured with $H \parallel x$ and y, see Supplementary Fig. 2) originate from the Van Vleck paramagnetism and can be well understood in principle through the single-ion Hamiltonian. At zero applied field $\mathbf{H}$ = (0, 0, 0), 14 CEF doublets of the eigenvectors form with E_1 = E_2, ..., E_{27} = E_{28}, which are protected by the time-reversal symmetry of the system in accordance with Kramers' law. In the subspace of the ground-state CEF doublet, denoted by $|E_1\rangle$ and $|E_2\rangle$, the matrix element of the magnetic moment can be expressed as $m_{jj'}^{\alpha} = \langle E_j|2s^{\alpha}+L^{\alpha}|E_{j'}\rangle$, j, j' = 1, 2. Diagonalizing the matrix $\mathbf{m}^{\alpha}$ yields two eigenvalues, $-g^{\alpha}/2$ and $g^{\alpha}/2$, from which the g factor g^{α} can be obtained.

From least-squares fitting the experimental magnetic susceptibilities (see Supplementary Fig. 2) and g factors (with $g_{\rm e}^{x'} = g^x = 0$, $g_{\rm e}^{y'} = g^z = 11.04$, $g_{\rm e}^{z'} = g^y = 0$), we obtain $B_2^0 = 2.50$ meV, $B_2^2 = 3.14$ meV, $B_4^0 = -0.336$ meV, $B_4^2 = -1.22$ meV, $B_4^4 = -2.61$ meV, $B_6^0 = -0.00266$ meV, $B_6^2 = 0.191$ meV, $B_6^4 = 0.340$ meV, $B_6^6 = 0.578$ meV, and the calculated g factors, $g_{\rm c}^{x'} = 0.0$, $g_{\rm c}^{y'} = 11.04 \sim g^z$, $g_{\rm c}^{z'} = 0.0$. At low temperatures and low applied fields, the magnetism of α-CoV_2O_6 is primarily determined by the two lowest-lying single-ion states ($|E_1\rangle$ and $|E_2\rangle$), which are well-separated from other excited CEF states with an energy gap of $E_3 - E_1 \sim 140$ K (see inset of Supplementary Fig. 2).

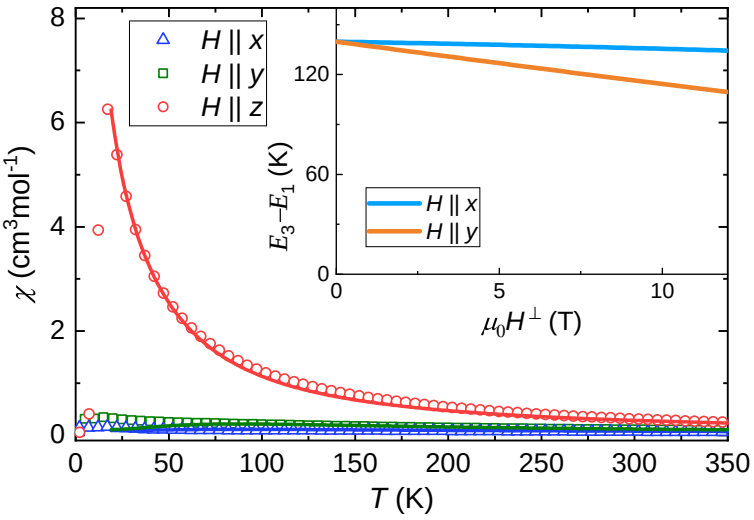

Supplementary Fig. 2 | Single-ion crystal field and spin-orbit couplings. Temperature dependence of the magnetic susceptibilities measured at 1 T applied along the x, y, z axes. The colored lines show the least-square fit above $T_{\rm N} \sim 14$ K by using the single-ion Hamiltonian of Supplementary Eq. (2). The inset presents the calculated energy gaps between the second-excited and ground-state single-ion states, $E_3 - E_1$, in transverse magnetic fields applied along the x and y axes.

At non-zero applied field, the ground-state CEF Kramers doublet is lifted with $E_2 > E_1$, due to the breaking of time-reversal symmetry. When a magnetic field is applied along the Ising (z) axis, the single-ion Hamiltonian of Supplementary Eq. (2) is represented as the well-known Zeeman term $\mathcal{H}_{\rm SI} = -\mu_0\mu_{\rm B}H^z g^z S^z + C$ in the subspace of $|E_1\rangle = |S^z = S\rangle$ and $|E_2\rangle = |S^z = -S\rangle$, where $E_2 - E_1 = \mu_0\mu_{\rm B}H^z g^z$, $C = (E_1 + E_2)/2$, $S = 1/2$, and

$$\mathbf{m}^x \sim \mathbf{m}^y \sim \begin{pmatrix} 0 & 0 \\ 0 & 0 \end{pmatrix}, \mathbf{m}^z \sim \frac{g^z}{2}\begin{pmatrix} 1 & 0 \\ 0 & -1 \end{pmatrix} = g^z S^z. \tag{4}$$

When the magnetic field is applied along the transverse (x or y) axis, in the subspace of $|E_1\rangle$ and $|E_2\rangle$ the magnetic moment is presented as

$$\mathbf{m}^x \sim \mathbf{m}^y \sim \begin{pmatrix} 0 & 0 \\ 0 & 0 \end{pmatrix}, \mathbf{m}^z \sim \frac{g^z}{2}\begin{pmatrix} 0 & -i \\ i & 0 \end{pmatrix} = g^z S^y. \tag{5}$$

The eigenstates of Supplementary Eq. (5) are also the effective spin-1/2 ($S = 1/2$) states,

$$|S^z = \pm S\rangle = \frac{1}{\sqrt{2}}(|E_1\rangle \pm i|E_2\rangle) \tag{6}$$

The single-ion Hamiltonian of Supplementary Eq. (2) can be expressed as the well-known transverse-field term $\mathcal{H}_{\rm SI} = (E_2 - E_1)(|E_2\rangle\langle E_2| - |E_1\rangle\langle E_1|)/2 + C = -\Gamma S^x + C$, in the subspace of the effective $S =$

1/2 states [10, 11]. Here, $\Gamma = E_2 - E_1$ is the transverse field, and $S^x = S(|S^z = S\rangle\langle S^z = -S| + |S^z = -S\rangle\langle S^z = S|) = -(|E_2\rangle\langle E_2| - |E_1\rangle\langle E_1|)/2$ is the effective S = 1/2 operator.

Supplementary Note 3. Classical Monte Carlo simulations at zero transverse field

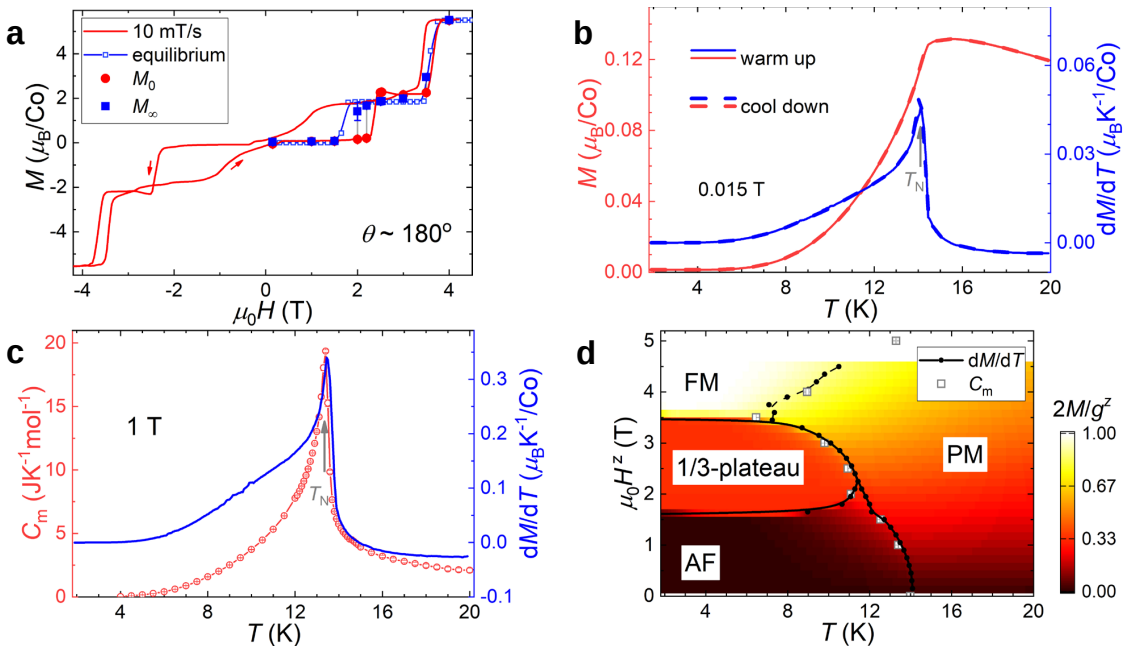

Supplementary Fig. 3 | Equilibrium-state magnetism via thermal annealing. a, Magnetization (M) of α-CoV_2O_6 measured with the magnetic field applied along the z (Ising) axis at 1.9 K. The red lines represent the hysteresis loop measured at a constant ramp rate of 10 mT/s, with the blue line showing the equilibrium-state M extracted from **d**. M_0 (red scatters) and M_∞ (blue scatters) are the magnetization at t = 0 and ∞ obtained from fitting the relaxation curves (see Supplementary Fig. 6b for example). **b**, Temperature dependence of equilibrium M and dM/dH measured at 15 mT. After achieving the steady field at 1.9 K (t = 0), we waited for 30 min before measuring M versus T by warming up to 20 K and subsequently cooling back down to 1.9 K. **c**, Temperature dependence of equilibrium specific heat and dM/dH measured at 1 T. The critical temperatures T_N are indicated in **b** and **c**. **d**, Equilibrium M measured by sweeping temperature at steady fields after allowing sufficient time for relaxation. The phase boundaries are determined based on the equilibrium dM/dH and specific heat measurements, and the different phases, including interchain antiferromagnetic (AF), up-up-down 1/3-plateau, fully-polarized ferromagnetic (FM), and high-T paramagnetic (PM) phases, are indicated. Error bars, 1σ s.e.

The magnetic structures of α-CoV_2O_6 at low temperatures and various applied magnetic fields were extensively studied using neutron diffraction measurements [4]. Saúl reported a comprehensive study of the magnetic interactions using density functional theory (DFT) and Monte Carlo (MC) calculations [5], which exhibited qualitative agreement with the experimentally observed magnetic structures. However, the

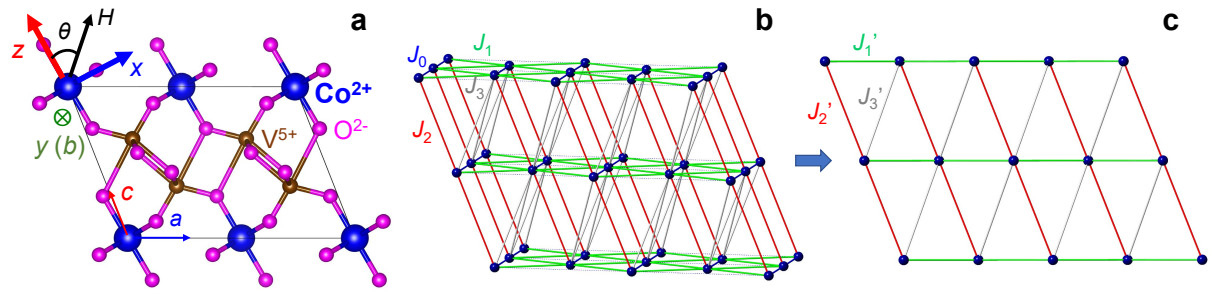

Supplementary Fig. 4 | Effective spin-1/2 interactions in α-CoV_2O_6. a, Crystal structure of α-CoV_2O_6, viewed along the b axis. The thin lines show the unit cell and the coordinate system for the spin components is established. **b**, First (J_0, |Co-Co|$_0 \sim 3.5$ Å), second (J_1, |Co-Co|$_1 \sim 4.9$ Å), third (J_2, |Co-Co|$_2 \sim 6.6$ Å), and fourth (J_3, |Co-Co|$_3 \sim 6.8$ Å) nearest neighbor Ising interactions. **c**, Due to the dominant ferromagnetic intrachain coupling J_0, all spins in each chain (along the b axis) are ordered (either up or down) at the ground state. As a result, the system can be approximated as a two-dimensional triangular lattice with modified couplings $J_1' = 2J_1$, $J_2' = J_2$, and $J_3' = 2J_3$, in the presence of a low transverse field $|\Gamma| \ll |J_0|$.

thermodynamic properties of α-CoV_2O_6 have not been fully reproduced and the Hamiltonian parameters are still not fully refined. This is due to the presence of complex metastable states below ~ 6 K, as indicated by the observed magnetic hysteresis (see Supplementary Fig. 3a) [3, 12]. To obtain equilibrium-state thermodynamic data, we allowed the spin system to fully relax for a time t longer than the intrinsic relaxation time τ (i.e., thermal annealing time), which is commonly less than ~1,000 s above $\sim$ 1.9 K (see Supplementary Fig. 6). The magnetization M, measured after waiting 30 min for the system to relax, shows no evident magnetic hysteresis (see Supplementary Fig. 3b), and the dM/dH and specific heat $C_{\rm m}$ only exhibit a sharp peak (see Supplementary Fig. 3b,c), consistent with theoretical predictions of equilibrium-state properties [5]. This confirms the approach to thermodynamic equilibrium in our measurements.

In this work, we start from the previously reported effective spin-1/2 Hamiltonian in zero transverse field [5] (see Supplementary Fig. 4b),

$$\mathcal{H} = J_0 \sum_{\langle i,i_0\rangle} S_i^z S_{i_0}^z + J_1 \sum_{\langle i,i_1\rangle} S_i^z S_{i_1}^z + J_2 \sum_{\langle i,i_2\rangle} S_i^z S_{i_2}^z + J_3 \sum_{\langle i,i_3\rangle} S_i^z S_{i_3}^z - \mu_0\mu_{\rm B} H^z g^z \sum_i S_i^z, \qquad (7)$$

where S_i^z represents the component of the magnetic moment along the z axis on the ith site, $g^z \sim 11.04$ is the g factor determined from the magnetization (see Supplementary Fig. 5a), and the couplings beyond fourth-nearest neighbors are neglected based on the DFT calculation, which shows $|J_n| \leq 0.02|J_0|$ for $n \geq 4$ [5]. To balance computational costs and potential finite-size effects, we initially conducted standard Metropolis MC simulations above 1.9 K on a 1,296-site cluster with periodic boundary conditions (PBC). The cluster had dimensions N_a = 6, N_b = 18, N_c = 6, where N_a, N_b, and N_c represent the numbers of unit cells along

Supplementary Table 1 | Ising spin Hamiltonian parameters of α-CoV_2O_6. Previously reported theoretical parameters (no. 1) [5] and those obtained by fitting the equilibrium-state magnetization (no. 2, see Supplementary Fig. 5a). The standard deviation $\sigma_{\rm d}$ is defined using the experimental magnetization $M_k^{\rm e}$, calculated magnetization $M_k^{\rm c}$, and the number of data points N.

interactions	no. 1 [5]	no. 2 (this work)
intrachain J_0	-29.8 K	-30.73 K
interchain J_1	4.9 K	3.60 K
interchain J_2	10.6 K	14.21 K
interchain J_3	2 K	2.55 K
$\sigma_{\rm d} = \sqrt{\sum_k (M_k^{\rm e} - M_k^{\rm c})^2/N}$	0.47 $\mu_{\rm B}$/Co	0.08 $\mu_{\rm B}$/Co

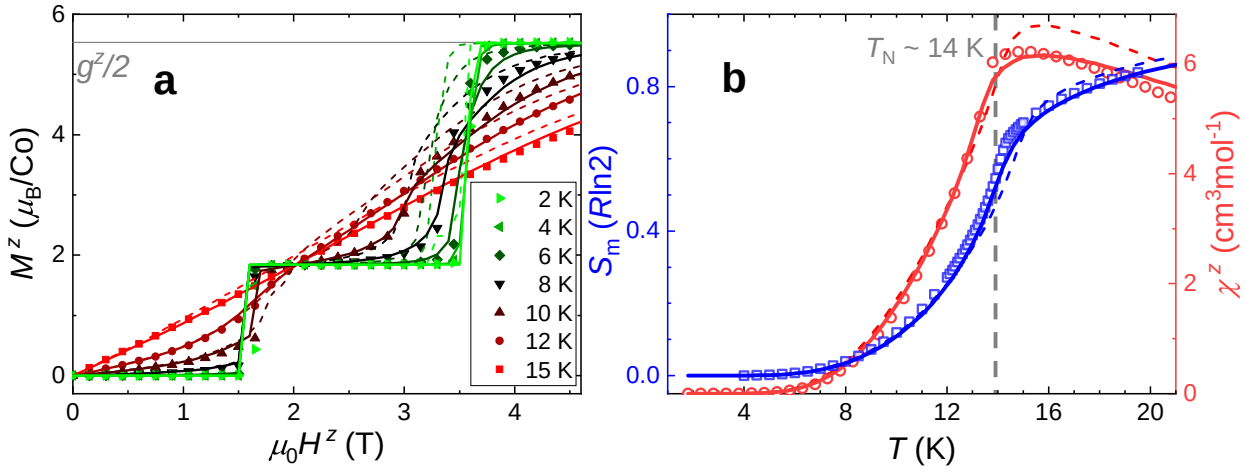

Supplementary Fig. 5 | Monte Carlo simulations of the equilibrium-state magnetism. a, Equilibrium magnetization of α-CoV_2O_6 (scatters), extracted from the data presented in Supplementary Fig. 3d. The dashed lines show the calculations using model no. 1 [5], while the solid lines represent the combined fit of the experimental data in model no. 2 (see Supplementary Tab. 1). **b**, Magnetic entropy ($S_{\rm m} = \int_{4{\rm K}}^{T} \frac{C_p({\rm Co}) - C_p({\rm Zn})}{T'} {\rm d}T'$, where $C_p({\rm Co})$ and $C_p({\rm Zn})$ are the zero-field specific heats measured on α-CoV_2O_6 and α-ZnV_2O_6, respectively) and dc susceptibility (measured at 1 T), along with calculations from model no. 1 (dashed lines) and model no. 2 (solid lines) for comparison.

the a, b, and c axes, respectively, with each unit cell containing two Co^{2+} spins. We computed the average values of thermodynamic observables at intervals of 4 Monte Carlo steps (MCS), after discarding the first 30,000 MCS for equilibration, and up to 50,000 MCS. By fitting the equilibrium magnetization above 1.9 K (see Supplementary Fig. 5a), we obtained the fully refined Hamiltonian parameters by minimizing

the standard deviation $\sigma_{\rm d}$ (see Supplementary Tab. 1 for model no. 2). Supplementary Fig. 5 shows that the refined model no. 2, with the significantly reduced $\sigma_{\rm d}$, reproduces the equilibrium magnetization, susceptibility, and entropy better than the previously reported model no. 1. Therefore, we propose that the effective spin-1/2 Hamiltonian of model no. 2 (see Supplementary Tab. 1) accurately describes the low-T magnetism of α-CoV_2O_6, without the need for any additional parameter tuning. This Hamiltonian gives rise to three well-defined ground states under different conditions: (1) When $|H^z|$ is less than $H^z_{\rm c1}$, the ground phase is the stripe AF state (see the left inset of Supplementary Fig. 7c) with an energy per site of $E_{\rm GS} = \frac{J_0}{4} - \frac{J_1}{2} - \frac{J_2}{4} + \frac{J_3}{2}$ (~ -11.76 K). (2) When $H^z_{\rm c1} < |H^z| < H^z_{\rm c2}$, the system enters the one-third magnetization plateau state (see the left inset of Supplementary Fig. 7d) with $E_{\rm GS} = \frac{J_0}{4} - \frac{J_1}{6} - \frac{J_2}{12} - \frac{J_3}{6} - \frac{\mu_0\mu_{\rm B}|H^z|g^z}{6}$. (3) When $|H^z|$ is greater than $H^z_{\rm c2}$, the spin system becomes fully polarized along the z axis with $E_{\rm GS} = \frac{J_0}{4} + \frac{J_1}{2} + \frac{J_2}{4} + \frac{J_3}{2} - \frac{\mu_0\mu_{\rm B}|H^z|g^z}{2}$. The critical longitudinal fields are given by $\mu_0 H^z_{\rm c1} = \frac{2J_1+J_2-4J_3}{\mu_{\rm B}g^z}$ ($\sim$ 1.5 T) and $\mu_0 H^z_{\rm c2} = \frac{2J_1+J_2+2J_3}{\mu_{\rm B}g^z}$ ($\sim$ 3.6 T).

To simulate the magnetic dynamics of α-CoV_2O_6 at low temperatures, we performed MC calculations using model no. 2 on a larger cluster of 28,800 sites with PBC. The cluster had dimensions of N_a = 12, N_b = 50, and N_c = 24, and we ran simulations for up to 50,000 MCS (Extended Data Fig. 2). We calculated the fictitious "time" (in MCS) dependence [13, 14] of magnetization on another 3,600-site cluster (with PBC and dimensions of N_a = 3, N_b = 100, and N_c = 6) using random initial states for up to 5,000 MCS, and evaluated over 50 independent samples, in Supplementary Fig. 6. Based on a comparison with experimental data (Supplementary Fig. 6c,d), we estimated that 1 MCS corresponds to approximately 10 s.

Based on the classical MC simulations described above, the low-T ($T \ll T_{\rm N}$) magnetic properties of α-CoV_2O_6 can be summarized as follows: (i) After long relaxation times, the correlation length along the chain (b axis) is much larger than that along the triangular lattice (ac plane) at $\mu_0 H^z$ = 0 and 2 T, which is attributed to the dominant intrachain FM coupling $J_0 \sim -30$ K. (ii) At low temperatures, the presence of low-energy topological excitations, such as vortices, antivortices, and vortex-antivortex pairs, can effectively confine domain walls, leading to remarkably long lifetimes ($\geq$ 20,000 MCS $\sim$ 60 hours). Our MC simulations indicate that introducing structural defects to confine magnetic domain walls is unnecessary, as good agreement with experimental data is achieved without any structural disorder (Supplementary Fig. 6). (iii) After 10 MCS, the density of excitations and the residual energy ($E - E_{\rm GS}$) are typically higher at $\mu_0 H^z$ = 2 T compared to 0 T. The relaxation time exhibits a maximum at $\mu_0 H^z \sim$ 2 T, consistent with the experimental results (see Supplementary Fig. 6c). In sharp contrast, at $\mu_0 H^z$ = 4 T the spin system quickly relaxes to its ground state after only 3-4 MCS. This suggests that the interchain spin frustration plays an important role in the extremely slow dynamics observed at low temperatures. (iv) The relaxation processes of different samples last for different times (see Supplementary Fig. 6a), leading to a distribution of the

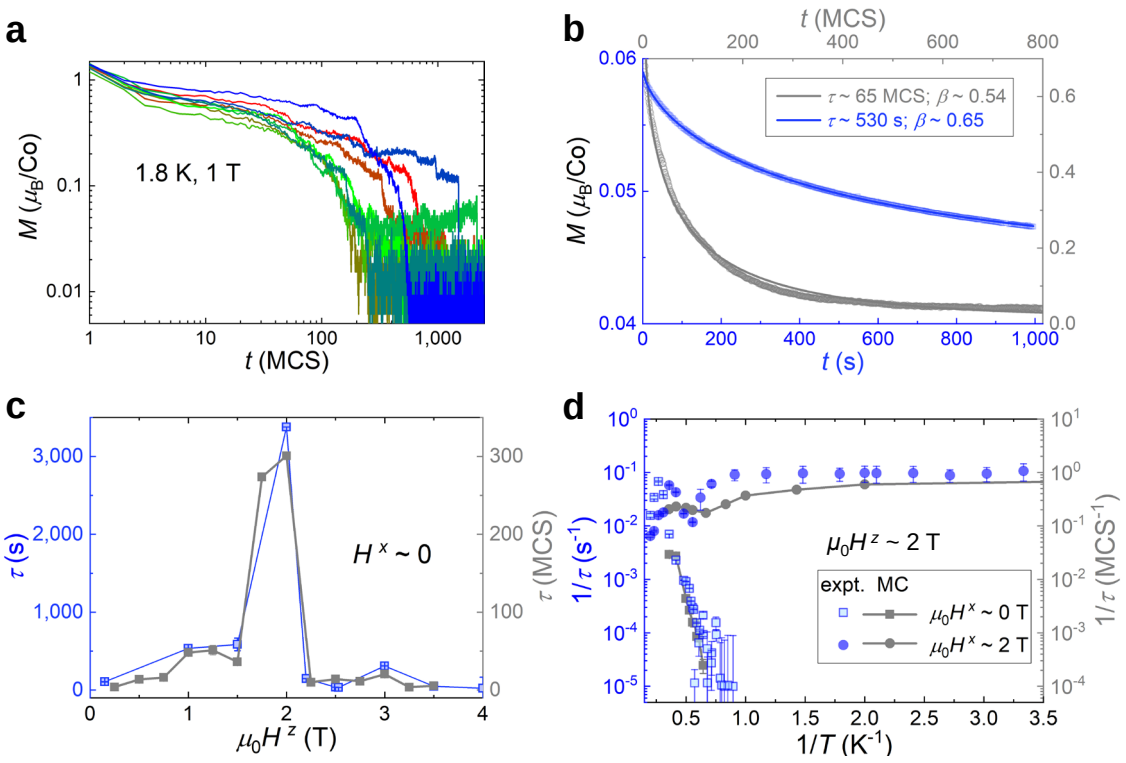

Supplementary Fig. 6 | Comparing magnetic dynamics in experiment and theory. a, Magnetization (M) of 9 randomly selected samples as a function of Monte Carlo step (MCS), calculated at T = 1.8 K and $\mu_0 H^z$ = 1 T. **b**, Time (t) dependence of M measured at T = 1.8 K and $\mu_0 H^z$ = 1 T (blue scatters). We collected magnetization data at t = 0, as soon as $\mu_0 H^z$ had stabilized at the set value from -4.2 T with a ramp rate of 10 mT/s. The MC M (gray scatters) was calculated on the 3,600-site cluster using random initial states by evaluating over 50 independent samples. The blue and gray lines present the stretched-exponential fits to the experimental and calculated data respectively, $M(t) = (M_0 - M_\infty)\exp[-(t/\tau)^\beta] + M_\infty$, where τ is the relaxation time, β is the stretching exponent, M_0 and M_∞ are the initial and final magnetization respectively. **c**, Longitudinal field ($\mu_0 H^z$) dependence of measured (blue) and calculated (gray) relaxation times at 1.8 K and $H^x \sim 0$. **d**, Relaxation rates at the longitudinal magnetic field of $\mu_0 H^z \sim 2$ T, and at transverse magnetic fields of $\mu_0 H^x \sim 0$ and 2 T. The gay lines present the corresponding classical and quantum MC calculations in **c** and **d**. Error bars, 1σ s.e.

relaxation times (τ) and thus a stretched-exponential relaxation behavior [15] (e.g., see Supplementary Fig. 6b).

Supplementary Note 4. Quantum computations with low transverse fields

Exact diagonalization

In zero transverse field, the Ising spin Hamiltonian of α-CoV_2O_6 (Supplementary Eq. (7)) commutes with S_i^z operators, allowing classical MC simulations on large clusters to reproduce the low-T magnetic

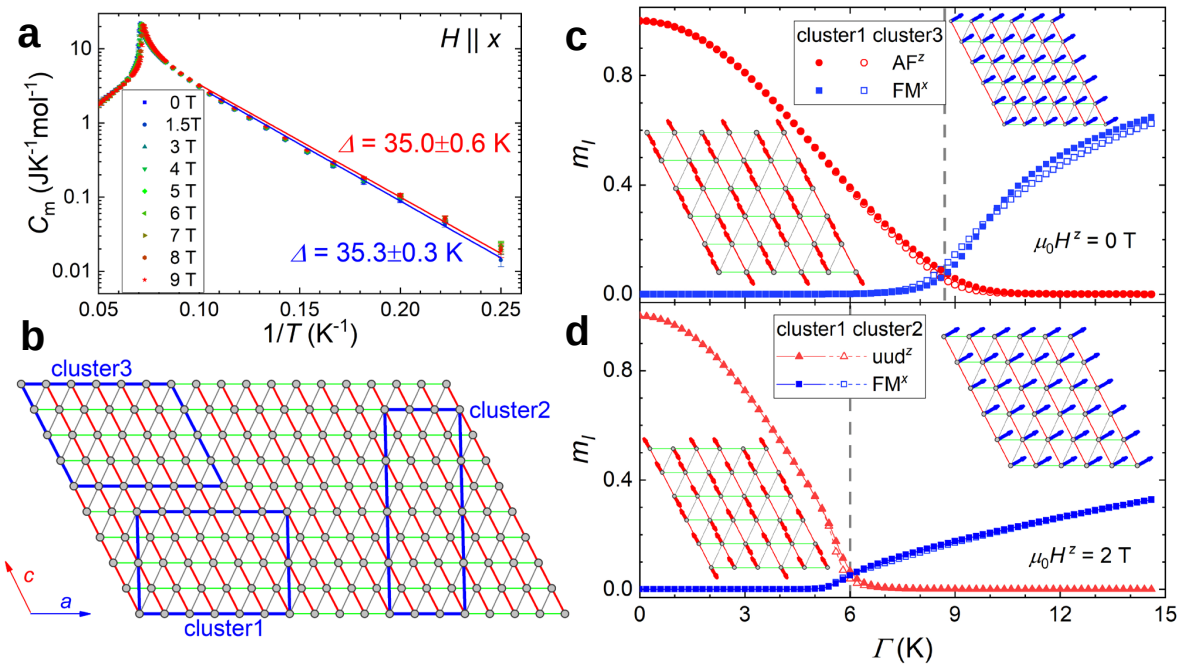

Supplementary Fig. 7 | Ground-state magnetism in transverse fields investigated by exact diagonalization. a, Gapped behavior in specific heat measurements under transverse magnetic fields (H^x), $C_{\rm m} \sim \exp(-\Delta/T)$. The gaps were fit to $\Delta = 35.3 \pm 0.3$ K and 35.0 ± 0.6 K at $\mu_0 H^x = 0$ T and 9 T, respectively, within the temperature range of 4-10 K. Alternatively, a power-law function can be used, but it only provides a good fit within a narrow range of 4-6 K, and the resulting power-law exponent of 6.4 ± 0.2 is unreasonably large. Error bars, 1σ s.e. **b**, The 24-chain clusters with different PBC used in the calculations. **c**, **d**, The transverse field (Γ) dependence of the ordering parameters (m_I) calculated at $\mu_0 H^z = 0$ and 2 T, respectively. The critical transverse fields are marked by dashed lines, and the corresponding magnetic structures of the triangular lattice (ac plane) are displayed in the insets. The dipole magnetic orders, including the antiferromagnetic (AF^z) and up-up-down (uud^z) orders, are characterized by $m_I = |\langle \mathrm{GS}|S_I^z|\mathrm{GS}\rangle|/S$, while the quantum paramagnetic phase (FM^x) is characterized by $m_I = \langle \mathrm{GS}|S_I^x|\mathrm{GS}\rangle/S$. Here, $|\mathrm{GS}\rangle$ represents the ground-state wavefunction, and $S = 1/2$.

behaviors (Supplementary Note 3). The nonzero transverse field terms, $\mathcal{H}_{\rm TF} = -\Gamma \sum_i S_i^x$, do not commute with the S_i^z operators, resulting in quantum tunnelling between states with $S_i^z = \pm 1/2$. However, this makes the computational cost much higher. According to the previous theoretical work [5] and our MC simulations, all Ising spins in each chain at $\Gamma = 0$ are aligned due to the dominant intrachain ferromagnetic coupling ($|J_0| \gg |J_n|$, n = 1, 2, 3). This alignment is protected by an energy gap of $\sim$ 35 K $\sim |J_0|$, as shown in Supplementary Fig. 7a, resulting in only two states for each chain, all spin up or down, at low temperatures. Under weak transverse fields ($|\Gamma| \ll |J_0|$), it is expected that all Ising spins in each chain remain aligned at low temperatures, and $\mathcal{H}_{\rm TF}$ mainly competes with the weak interchain couplings (J_1, J_2, and J_3) in α-CoV_2O_6, highly similar to the case of $Ca_3Co_2O_6$ [16]. As a result, the three-dimensional (3D)

spin Hamiltonian can be reduced to a 2D triangular lattice with frustrated interactions ($J_1' = 2J_1$, $J_2' = J_2$, $J_3' = 2J_3$),

$$\mathcal{H} \approx J_1' \sum_{\langle I,I_1\rangle} S_I^z S_{I_1}^z + J_2' \sum_{\langle I,I_2\rangle} S_I^z S_{I_2}^z + J_3' \sum_{\langle I,I_3\rangle} S_I^z S_{I_3}^z - \mu_0\mu_{\rm B} H^z g^z \sum_I S_I^z - \Gamma \sum_I S_I^x, \qquad (8)$$

where S_I presents the spin operator of an arbitrary Co^{2+} ion in the Ith chain. The 2D Hamiltonian represented in Eq. (8) also yields three different ground phases separated by two critical longitudinal fields, $\mu_0 H_{\rm c1}^z = \frac{J_1'+J_2'-2J_3'}{\mu_{\rm B} g^z}$ and $\mu_0 H_{\rm c2}^z = \frac{J_1'+J_2'+J_3'}{\mu_{\rm B} g^z}$, in zero transverse field, parallel to the original 3D Hamiltonian presented in Eq. (7). The ground-state wavefunctions were calculated using the Lanczos diagonalization algorithm on 24-chain clusters with PBC, utilizing 80 Lanczos steps and 20 random initial states [17–20]. The calculations did not reveal any significant finite-size effects (see Supplementary Fig. 7).

At Γ = 0 K, the ground states exhibit the interchain antiferromagnetic (AF^z) and up-up-down (uud^z) orders with the ordering parameters of 1 at $\mu_0 H^z$ = 0 and 2 T, respectively (Supplementary Fig. 7c,d), as predicted by the classical MC simulations [5] (also see above). As Γ increases, the dipole magnetic orders (AF^z and uud^z) are gradually suppressed. At the critical transverse field of $\Gamma_{\rm c}$, the interchain antiferromagnetic (AF^z) or up-up-down (uud^z) ordering parameter approaches zero, while the ordering parameter of the ferromagnetic component (FM^x) $m_I = \langle {\rm GS}|S_I^x|{\rm GS}\rangle/S$ starts to grow. At $\Gamma > \Gamma_{\rm c}$, the classical Ising spin ordering is fully suppressed, and the system enters the quantum paramagnetic phase, known as the FM^x phase. In this phase, the system exhibits a spontaneous transverse magnetization along the x axis due to quantum fluctuations, which is the hallmark of the FM^x phase. Our exact diagonalization calculations reveal a significant reduction in the critical value $\Gamma_{\rm c}$ from 8.7 ± 0.1 K at $\mu_0 H^z$ = 0 T (Supplementary Fig. 7c) to 6.0 ± 0.1 K at $\mu_0 H^z$ = 2 T (Supplementary Fig. 7d). However, these critical transverse fields are still much larger than the maximum value of Γ ($\sim$ 0.1 K) achieved in our experiments by applying a transverse magnetic field of $\sim$10 T along the b axis. In this study, the transverse field of $\Gamma < 0.1$ K is considered too weak to significantly alter the lowest-energy configurations.

Integral-path Monte Carlo simulations

We conducted quantum Monte Carlo (QMC) computations to study the low-T magnetism of α-CoV_2O_6 (using model no. 2, see Supplementary Tab. 1) under a low transverse field on a large scale. At a finite temperature, we present the thermal density matrix of the transverse-field part in the integral path as

$$\exp(\frac{\Gamma S_I^x}{k_{\rm B}T}) = \cosh(\frac{\Gamma}{2k_{\rm B}T})[I_{2\times2} + 2\tanh(\frac{\Gamma}{2k_{\rm B}T})S_I^x], \qquad (9)$$

where $I_{2\times2}$ is the 2×2 identity matrix and $S_I^x = \sigma_I^x/2$ is the effective spin-1/2 operator ($\sigma_I^x = \begin{pmatrix} 0 & 1 \\ 1 & 0 \end{pmatrix}$ is the Pauli matrix acting on the Ith chain). Similarly, the thermal density matrix of the effective "interlayer" part

(along $\langle I', I'_0\rangle$) can be expressed as

$$\exp(\frac{-J'_0 S^z_{I'} S^z_{I'_0}}{k_{\rm B}T}) = \exp(\frac{-J'_0}{4k_{\rm B}T}) \begin{pmatrix} 1 & e^{\frac{J'_0}{2k_{\rm B}T}} \\ e^{\frac{J'_0}{2k_{\rm B}T}} & 1 \end{pmatrix} = \exp(\frac{-J'_0}{4k_{\rm B}T})[I_{2\times 2} + 2\exp(\frac{J'_0}{2k_{\rm B}T}) S^x_I]. \quad (10)$$

To represent Eq. (9) with Eq. (10), we obtain $\tanh(\frac{\Gamma}{2k_{\rm B}T}) = \exp(\frac{J'_0}{2k_{\rm B}T})$ and thus $J'_0 = 2k_{\rm B}T \ln[\tanh(\frac{\Gamma}{2k_{\rm B}T})]$. The constant pre-factors in Eqs. (9) and (10) are automatically eliminated when calculating any observables, given by $\langle O\rangle = \frac{{\rm Tr}(O e^{-\frac{\mathcal{H}}{k_{\rm B}T}})}{{\rm Tr}(e^{-\frac{\mathcal{H}}{k_{\rm B}T}})}$. Therefore, the 2D Hamiltonian with transverse-field terms (Eq. (8)) can be equivalent to a 3D Hamiltonian with the ferromagnetic coupling in the third (Trotter) direction (J'_0) [13, 21],

$$\mathcal{H} \approx J'_1 \sum_{\langle I', I'_1\rangle} S^z_{I'} S^z_{I'_1} + J'_2 \sum_{\langle I', I'_2\rangle} S^z_{I'} S^z_{I'_2} + J'_3 \sum_{\langle I', I'_3\rangle} S^z_{I'} S^z_{I'_3} - \mu_0 \mu_{\rm B} H^z g^z \sum_{I'} S^z_{I'} + J'_0 \sum_{\langle I', I'_0\rangle} S^z_{I'} S^z_{I'_0}, \quad (11)$$

$\langle S^z_I\rangle = \frac{1}{N_{b'}} \sum_{I'\in I} \langle S^z_{I'}\rangle$ is used to calculate the observables. The Trotter error is controlled by $(\frac{1}{k_{\rm B}T N_{b'}})^2$, where $N_{b'}$ is the number of Trotter replicas along the "bond" $\langle I, I_0\rangle$. Our QMC computations used a 28,800-site cluster with PBC and dimensions of $N_{b'}$ = 50, N_a = 12, and N_c = 24 (Fig. 4 and Extended Data Fig. 4 in the main text). The simulation of relaxation rate agrees with the experimental data (see Supplementary Fig. 6d).

Supplementary Note 5. Technical details of Faraday force magnetometer and heat transport measurements

Below 2 K, the magnetization (M, in $\mu_{\rm B}$/Co) of α-CoV_2O_6 (single crystals, $\sim$ 1 mg) was measured using a high-resolution Faraday force magnetometer in a ^{3}He-^{4}He dilution refrigerator (KELMX-400, Oxford Instruments) [22, 23]. The applied main magnetic fields (H) and field gradients (dH/dl) were generated by the superconducting coils (in INTA-LLD-S12/14, Oxford Instruments), and the electrical capacitance was measured using a digital capacitance bridge (AH-2500A, Andeen-Hagerling, Inc.) with the three-terminal method. The change in the inverse electrical capacitance is given by,

$$\Delta(\frac{1}{C}) = \frac{\Delta d}{\epsilon_0 A} = \frac{\mu_0 N_{\rm A} \mu_{\rm B} M {\rm d}H/{\rm d}l}{k_{\rm eff}\epsilon_0 A}, \quad (12)$$

where ϵ_0 represents the electric permittivity of vacuum, A is the area of the top (smaller) plate, Δd denotes the variation in the gap, and $k_{\rm eff}$ represents the effective spring coefficient in Hook's law (see Supplementary Fig. 8a). Therefore, we obtained the magnetization by measuring the inverse electrical capacitance (see Supplementary Fig. 8b). By scaling the results to the magnetization measured by MPMS (see Supplementary Fig. 8c), we got $k_{\rm eff} \sim 3.4\times 10^3$ N/m at low temperatures, slightly higher than the value of $\sim 2.5\times 10^3$ N/m measured at room temperature.

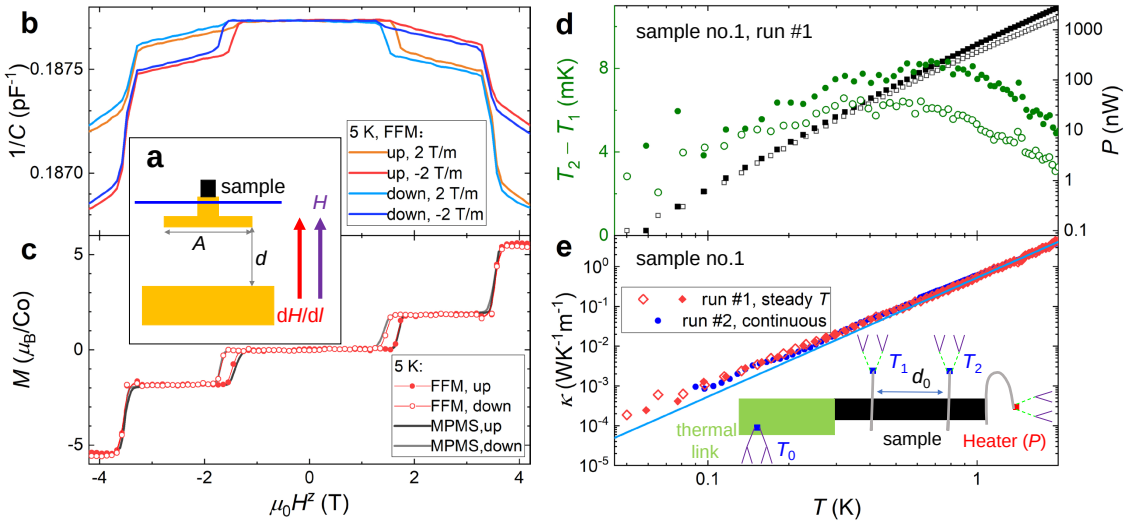

Supplementary Fig. 8 | Faraday force magnetometer and heat transport measurements on single crystals of α-CoV_2O_6. a, Schematic diagram of the Faraday force magnetometer (FFM). **b**, Inverse electrical capacitance measured by sweeping the magnetic field (applied along the z axis) up and down at different magnetic field gradients at 5 K. **c**, Field dependence of magnetization measured by FFM and MPMS at 5 K. **d**, The heating power applied to the sample and the resulting temperature difference between the two thermometers ($T_2 - T_1$, see inset of **e**). **e**, Thermal conductivity data measured in steady-T and continuous-T sweep modes (run #1 and #2). A power-law fit to the run #1 data is represented by the line, $\kappa = \gamma T^{\alpha'}$, where $\alpha' = 2.99(2)$ and $\gamma = 0.524(4)$ $WK^{-4}m^{-1}$. The inset illustrates a schematic diagram of the experimental setup employed for thermal conductivity measurements.

The low-temperature (down to $\sim$ 50 mK) thermal conductivity (κ, in $WK^{-1}m^{-1}$) measurements were conducted using a standard four-wire steady-state method on three single crystals of α-CoV_2O_6 in the dilution refrigerator [24]. Two samples have roughly rectangular shapes of $0.11\times0.45\times1.0$ mm^3 (sample no. 1) and $0.11\times0.56\times1.2$ mm^3 (sample no. 3), with the long edges along the b (chain) axis, whereas the sample no. 2 has dimensions of $0.15\times0.6\times1.6$ mm^3 with the long edge along the a axis (along the triangular plane). The silver wires of the two thermometers (T_1 and T_2) and heater (P) were attached to the surfaces of the samples with silver paint (see inset of Supplementary Fig. 8e), to let the heat flow along the spin chain (samples nos. 1,3) or along the a axis in the triangular plane (sample no. 2). These two RuO_2 chip thermometers (T_1 and T_2, RX-102A-BR, LakeShore) were *in situ* calibrated against a reference (T_0, RX-102B-RS-0.02B, LakeShore, calibrated down to 20 mK) at each applied magnetic field, by turning off the heater (i.e., at $P = 0$). The thermal conductivity is obtained as

$$\kappa(T = \frac{T_2 + T_1}{2}) = \frac{d_0 P}{A_0(T_2 - T_1)}, \tag{13}$$

where d_0 is the distance between the two thermometers (T_1 and T_2), A_0 represents the cross-section area

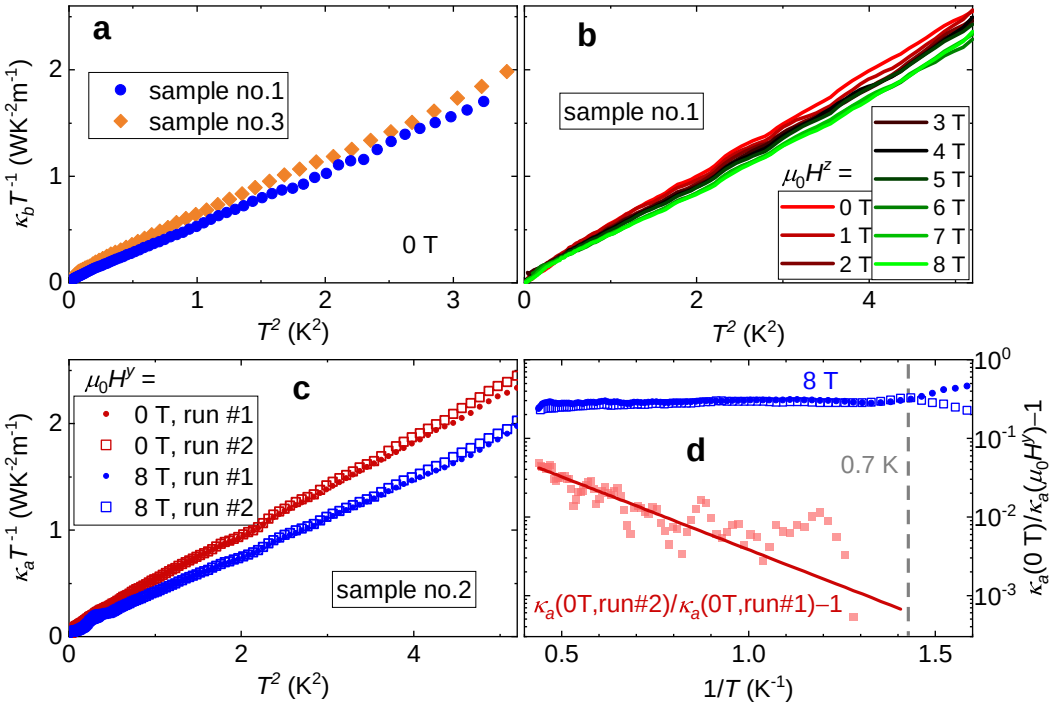

Supplementary Fig. 9 | Extended thermal conductivity data of α-CoV_2O_6. a, Zero-field thermal conductivity measured along the b axis (κ_b) on two samples (nos. 1 and 3). **b**, The data measured on sample no. 1 under various longitudinal magnetic fields. **c**, Thermal conductivity measured along the a axis (κ_a) on sample no. 2 under transverse magnetic fields of $\mu_0 H^y$ = 0 and 8 T. We measured the data at 1 T intervals from 0 to 8 T twice, with the first measurement designated as run $\#1$ (0 $\rightarrow$ 8 T) and the second as run $\#2$ (0 $\rightarrow$ 8 T, again). **d**, κ_a(0 T)/κ_a($\mu_0 H^y$)-1. The red line displays the Arrhenius fit to the experimental data of κ_a(0 T, run $\#2$)/κ_a(0 T, run $\#1$)-1 above $\sim$ 0.7 K, $\propto \exp(-\Delta E/T)$, with ΔE = 4.3$\pm$0.3 K.

of the single-crystal sample, T_1 and T_2 are the measured temperatures of the thermometers, and P the measured power of the heater (see Supplementary Fig. 8d). d_0 = 0.40, 0.66, 0.50 mm, A_0 = 0.050, 0.090, 0.062 mm^2, for samples nos. 1, 2, 3 respectively, were determined by using a microscope.

The final thermal conductivity is independent of the excited power P (see Supplementary Fig. 8d,e), suggesting good linear response, and is also independent of different measurement modes (Supplementary Fig. 8e). No significant sample dependence of κ_b between samples nos. 1 and 3 was observed (Supplementary Fig. 9a). As shown in Supplementary Fig. 9b κ_b is less sensitive to longitudinal magnetic fields H^z than κ_a to transverse magnetic fields H^y (Supplementary Fig. 9c). Here, κ_a and κ_b are the thermal conductivities measured along the a and b axes, respectively. The slight suppression of κ_b by H^z can be attributed to increased inelastic phonon-spin scattering, which is enhanced by closing the spin gap (see Extended Data Fig. 1c) [25]. Moreover, Supplementary Fig. 9c shows that κ_a has a weak dependence on run

sequences. Long-term exploration (about 10 days) at low temperatures ($\leq$ 2.3 K) under transverse magnetic fields (up to $\mu_0 H^y$ = 8 T) only slightly increases κ_a, suggesting that the magnetic crystal is approaching its equilibrium state. In this work, we utilized the most recently measured κ_a at zero field (in run #2), which had the highest values for almost the entire temperature range (see Supplementary Fig. 9c), as the pure phonon thermal conductivity $\kappa_{\rm p}$. As explained in the main text, we used κ_b(0 T, run #2)/$\kappa_b(\mu_0 H^y)-1$ to approximate $\tau_{\rm pp}/\tau_{\rm ps}$, where $\tau_{\rm pp}^{-1}$ and $\tau_{\rm ps}^{-1}$ are the pure phonon and phonon-spin scattering rates, respectively. $\tau_{\rm pp}$ is expected to be nearly independent of temperature and applied magnetic field below 2.3 K ($\ll$ Debye temperature of $\sim$ 160 K). Hence, κ_b(0 T, run #2)/$\kappa_b(\mu_0 H^y)-1$ is an approximate representation of the spin fluctuations around magnetic domain walls, as the system undergoes annealing by flipping spins near the domain walls. As shown in Supplementary Fig. 9d, κ_b(0 T, run #2)/κ_b(0 T, run #1)-1 exhibits a thermally activated Arrhenius behavior above $\sim$ 0.7 K, $\propto \exp(-\Delta E/T)$, where ΔE = 4.3$\pm$0.3 K represents the zero-field barrier energy. In contrast, κ_b(0 T, run #2)/$\kappa_b(\mu_0 H^y)-1$ ($\mu_0 H^y \geq$ 1 T) remains almost constant throughout the same temperature range, suggesting the emergence of quantum spin fluctuations induced by the transverse field.

Supplementary References

[1] Z. He, J.-I. Yamaura, Y. Ueda, and W. Cheng, "CoV_2O_6 single crystals grown in a closed crucible: unusual magnetic behaviors with large anisotropy and $\frac{1}{3}$ magnetization plateau," J. Am. Chem. Soc. **131**, 7554–7555 (2009).

[2] Z. He and W. Cheng, "Magnetic phase diagram of an Ising spin-chain system α-CoV_2O_6 with 1/3 magnetization plateau," J. Magn. Magn. Mater. **362**, 27–30 (2014).

[3] C. B. Liu, Z. Z. He, S. L. Wang, M. Yang, Y. Liu, Y. J. Liu, R. Chen, H. P. Zhu, C. Dong, J. Z. Ke, Z. W. Ouyang, Z. C. Xia, and J. F. Wang, "Field-induced magnetic transitions and strong anisotropy in α-CoV_2O_6 single crystal," J. Phys.: Condens. Matter **31**, 375802 (2019).

[4] M. Lenertz, J. Alaria, D. Stoeffler, S. Colis, A. Dinia, O. Mentré, G. André, F. Porcher, and E. Suard, "Magnetic structure of ground and field-induced ordered states of low-dimensional α-CoV_2O_6: Experiment and theory," Phys. Rev. B **86**, 214428 (2012).

[5] A. Saúl, D. Vodenicarevic, and G. Radtke, "Theoretical study of the magnetic order in α-CoV_2O_6," Phys. Rev. B **87**, 024403 (2013).

[6] Y. Li, D. Adroja, R. I. Bewley, D. Voneshen, A. A. Tsirlin, P. Gegenwart, and Q. Zhang, "Crystalline electric-field randomness in the triangular lattice spin-liquid $YbMgGaO_4$," Phys. Rev. Lett. **118**, 107202 (2017).

[7] https://docs.mantidproject.org/nightly/concepts/CrystalField.html.

[8] J. Kanamori, "Theory of the magnetic properties of ferrous and cobaltous oxides, I," Prog. Theor. Phys. **17**, 177–196 (1957).

[9] J. A. Ringler, A. I. Kolesnikov, and K. A. Ross, "Single-ion properties of the transverse-field Ising model material $CoNb_2O_6$," Phys. Rev. B **105**, 224421 (2022).

[10] Y. Li, S. Bachus, H. Deng, W. Schmidt, H. Thoma, V. Hutanu, Y. Tokiwa, A. A. Tsirlin, and P. Gegenwart, "Partial up-up-down order with the continuously distributed order parameter in the triangular antiferromagnet $TmMgGaO_4$," Phys. Rev. X **10**, 011007 (2020).

[11] Y. Li, Q.-Y. Li, W. Li, T. Liu, D. J. Voneshen, P. K. Biswas, and D. Adroja, "Spin dynamics and Griffiths singularity in the random quantum Ising magnet $PrTiNbO_6$," npj Quantum Mater. **6**, 34 (2021).

[12] M. Nandi and P. Mandal, "Magnetic and magnetocaloric properties of quasi-one-dimensional Ising spin chain CoV_2O_6," J. Appl. Phys. **119**, 133904 (2016).

[13] G. E. Santoro, R. Martoňák, E. Tosatti, and R. Car, "Theory of quantum annealing of an Ising spin glass," Science **295**, 2427–2430 (2002).

[14] S. Kobayashi, H. Okano, T. Jogetsu, J. Miyamoto, and S. Mitsuda, "Domain growth kinetics in the isosceles triangular Ising antiferromagnet $CoNb_2O_6$," Phys. Rev. B **69**, 144430 (2004).

[15] P. Ocampo-Alfaro and H. Guo, "Cooling-rate dependence of the ground-state energy using microcanonical simulated annealing," Phys. Rev. E **53**, 1982–1985 (1996).

[16] A. D. King, C. D. Batista, J. Raymond, T. Lanting, I. Ozfidan, G. Poulin-Lamarre, H. Zhang, and M. H. Amin, "Quantum annealing simulation of out-of-equilibrium magnetization in a spin-chain compound," PRX Quantum **2**, 030317 (2021).

[17] J. Liu, B. Liu, L. Yuan, B. Li, L. Xie, X. Chen, H. Zhang, D. Xu, W. Tong, J. Wang, and Y. Li, "Frustrated magnetism of the triangular-lattice antiferromagnets α-CrOOH and α-CrOOD," New J. Phys. **23**, 033040 (2021).

[18] J. Liu, L. Yuan, X. Li, B. Li, K. Zhao, H. Liao, and Y. Li, "Gapless spin liquid behavior in a kagome Heisenberg antiferromagnet with randomly distributed hexagons of alternate bonds," Phys. Rev. B **105**, 024418 (2022).

[19] L. Yuan, Y. Zhao, B. Li, Y. Song, Y. Xia, B. Liu, J. Wang, and Y. Li, "Possible coexistence of short-range resonating valence bond and long-range stripe correlations in the spatially anisotropic triangular-lattice quantum magnet $Cu_2(OH)_3NO_3$," Phys. Rev. B **106**, 085119 (2022).

[20] F. Lu, L. Yuan, J. Zhang, B. Li, Y. Luo, and Y. Li, "The observation of quantum fluctuations in a kagome Heisenberg antiferromagnet," Comm. Phys. **5**, 272 (2022).

[21] T. D. Schultz, D. C. Mattis, and E. H. Lieb, "Two-dimensional Ising model as a soluble problem of many fermions," Rev. Mod. Phys. **36**, 856 (1964).

[22] Y. Shimizu, Y. Kono, T. Sugiyama, S. Kittaka, Y. Shimura, A. Miyake, D. Aoki, and T. Sakakibara, "Development of high-resolution capacitive Faraday magnetometers for sub-Kelvin region," Rev. Sci. Instrum. **92**, 123908 (2021).

[23] Y. Li, S. Bachus, B. Liu, I. Radelytskyi, A. Bertin, A. Schneidewind, Y. Tokiwa, A. A. Tsirlin, and P. Gegenwart, "Rearrangement of uncorrelated valence bonds evidenced by low-energy spin excitations in $YbMgGaO_4$," Phys. Rev. Lett. **122**, 137201 (2019).

[24] X. Hong, M. Behnami, L. Yuan, B. Li, W. Brenig, B. Büchner, Y. Li, and C. Hess, "Heat transport of the kagome Heisenberg quantum spin liquid candidate $YCu_3(OH)_{6.5}Br_{2.5}$: Localized magnetic excitations and a putative spin gap," Phys. Rev. B **106**, L220406 (2022).

[25] D. Watanabe, K. Sugii, M. Shimozawa, Y. Suzuki, T. Yajima, H. Ishikawa, Z. Hiroi, T. Shibauchi, Y. Matsuda, and M. Yamashita, "Emergence of nontrivial magnetic excitations in a spin-liquid state of kagomé volborthite," Proc. Natl. Acad. Sci. **113**, 8653–8657 (2016).